

Article

# Characteristics of Raindrop Size Distribution on the Eastern Slope of the Tibetan Plateau in Summer

Yingjue Wang, Jiafeng Zheng , Zhigang Cheng and Bingyun Wang

School of Atmospheric Sciences, Chengdu University of Information Technology, Chengdu 610225, China; 2017011201@cuit.edu.cn (Y.W.); chengzgj@cuit.edu.cn (Z.C.); bywang@cuit.edu.cn (B.W.)

\* Correspondence: zjf1988@cuit.edu.cn

Received: 6 April 2020; Accepted: 27 May 2020; Published: 28 May 2020



**Abstract:** Precipitation microphysics over the Tibetan Plateau (TP) remain insufficiently understood, due to the lack of observations and studies. This paper presents a comprehensive investigation of the raindrop size distribution (DSD) for rainfall that happened on the eastern slope of TP in summer. DSD differences between different rain types and under different rain rates are investigated. Confidential empirical relationships between the gamma shape and slope parameters, and between reflectivity and rain rate are proposed. DSD properties in this area are also compared with those in other areas. The results indicate that the stratiform and convective rains contribute to different rain duration and amount, with diverse rainfall macro- and microphysical properties. The rain spectra of two rain types can become broader with higher concentrations as the rain rate increases. DSDs in this area are different to those in other areas. The stratiform DSD is narrower than that in the non-plateau area. The two rain types of this area both have higher number concentrations for 0.437–1.625 mm raindrops than those of the mid-TP. The relationships of shape–slope parameters and reflectivity–rain rate in this area are also different from those in other areas. The rain spectra in this area can produce a larger slope parameter under the same shape parameter than in the mid-TP. The convective rain can produce a smaller rain rate under the same reflectivity. The accuracy proposed reflectivity–rain rate relationship in application to quantitative rainfall estimation is also discussed. The results show that the relationship has an excellent performance when the rain rate exceeds  $1 \text{ mm h}^{-1}$ .

**Keywords:** raindrop size distribution; stratiform and convective rains; empirical relationships; the eastern slope of Tibetan Plateau

## 1. Introduction

The Tibetan Plateau (TP) is the largest and highest plateau on the planet. It plays a vital role in the Asian climate and weather, owing to its powerful dynamic and thermal effects on the tropospheric atmosphere [1,2]. In summer, rainfall events over the TP are frequent, however, the reliability of numerical simulations over the TP is much lower than that in other plain areas, due to the lack of observations and insufficient knowledge of the microphysical processes and mechanisms of the precipitation. Thus, further observing and studying the microphysical characteristics of precipitation over the TP is of great importance.

As a vital aspect of precipitation microphysics, the raindrop size distribution (DSD) can reflect the number concentration of raindrops as a function of the diameter. The DSD can be directly measured by filter paper or disdrometer on the ground. Although the ground measurements cannot be the perfect representation of the real situation of the precipitation up in the air, the long-period DSD dataset, to some extent, can reveal the microphysical properties of different kinds of precipitation in different geographical locations [3–16]. Previous findings showed that different rain types possess different DSDs, and the convective rain commonly has wider raindrop spectra than the stratiform rain, with a

larger mean diameter and a higher total number concentration [17–19]. The maritime-like convection also generally possesses larger diameters and smaller number concentrations than the continental-like convection [4]. DSDs vary in space and time and over a range of scales, they can be apparently different, even in the same synoptic system, as a result of diverse water vapor and dynamic conditions [20–22]. Additionally, the observed DSD can be used to formulate the raindrop spectrum. In recent years, the most widely used mathematical formulation of DSDs is the three-parameter gamma model proposed by Ulbrich (1983) [7]. Fitting the gamma parameters and investigating their relationships in specific climatic regions can be useful to optimize the microphysical parameterization schemes of the regional numerical models [23–25]. A conventional technique for single-polarization weather radar to estimate the precipitation typically relies on the power law relationship between reflectivity ( $Z$ ,  $\text{mm}^6 \text{m}^{-3}$ ) and rain rate ( $R$ ,  $\text{mm h}^{-1}$ ) [26,27]. The  $Z$  and  $R$  are proportional to the sixth and third power of the raindrop diameter. Thus, investigating the DSD properties and deriving accurate coefficients of the  $Z$ - $R$  relationship is also crucial for improving radar quantitative precipitation estimation (QPE).

For the DSD study over the TP, limited works have been conducted because of the lack of observational data. Until 2013, an integrated observational experiment called the Third Tibetan Plateau Atmospheric Scientific Experiment (TIPEX-III) was launched by the China Meteorological Administration and other institutions [2]. One of the specific scientific goals of the TIPEX-III was to achieve a better understanding of microphysical processes of the cloud and precipitation over the TP [2,28]. The TIPEX-III deployed ground-based laser disdrometers for continuously observing rainfall properties and DSDs in the mid-TP (Nagqu,  $29.04^\circ \text{ N}$ ,  $100.30^\circ \text{ E}$ , 4,507 m asl) from July to August in 2013, 2014 and 2015. Based on the measurement collected from this experiment, rainfall properties have been studied by Chang et al. (2016), Chen et al. (2017) and Wu et al. (2017) [19,29,30]. The results concluded that raindrop spectra over the TP can be wider than those in basin areas, the widest spectra occur during 1700–1800 LST, due to the strong convection. The DSD exhibits a significant day/night variation; the daytime convection has broader DSDs with fewer small drops but more large drops than the nighttime case. The raindrop number concentration of stratiform rains in the mid-TP also has a more significant decrease with the increased diameter than that in South China, but convective rains can be the opposite. For precipitation physical processes over the mid-TP, Porcù et al. (2014) found that collisional breakup takes place for relatively lower rain rates than those at low altitudes [31].

Several abovementioned works have preliminarily revealed the DSD characteristics of rainfalls in the mid-TP. However, those findings cannot represent the whole situation on the TP, because the plateau has very complex geography and land features, which can lead to different rainfall properties in different areas. For example, compared to the mid-TP, the terrain and climate features of a transitional region of interest in this study, which locates between the plateau and the downstream basin at the eastern slope of TP, are quite different. Except for the rainfall events caused by similar synoptic systems as in the mid-TP, many precipitations can also be produced by local special synoptic systems, such as southwest vortex. More importantly, the rainfall microphysical properties over the eastern slope of TP have not been well investigated. In this paper, we attempt to present a comprehensive study of the DSD for rainfall that happened in this area in summer. In detail, the observation experiment, instrument and measurements, followed by methods of data quality control (QC) and rain type classification, are described in Section 2. The DSD characteristics for different rain rates and types are studied in Section 3. Relationships between three gamma parameters and between DSD integral quantities are also proposed. In Section 4, the results are compared with other studies and the uncertainties of the used methods are discussed. The conclusions are summarized in Section 5.

## 2. Data and Methods

### 2.1. Experiment, Instrument, and Measurements

To enhance the observation of cloud and precipitation over the eastern slope of TP, an observation experiment was performed by the Chinese Academy of Meteorological Sciences at Daocheng ( $29.04^\circ \text{ N}$ ,

100.30° E, 3800 m asl), China from 10 July to 31 August in 2016, as a continuation of the TIPEX-III. A key precipitation observation instrument deployed on the site is a ground-based disdrometer. Figure 1 shows the experiment location and the appearance of the disdrometer.

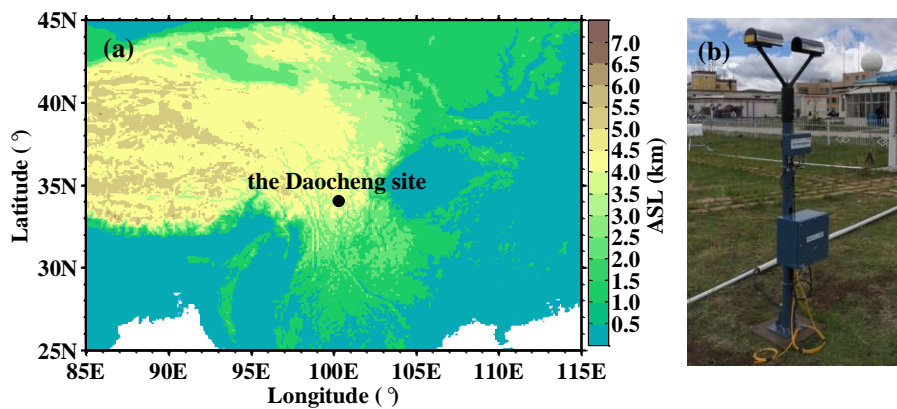


**Figure 1.** Location of the observation site (29.04° N, 100.30° E, 3800 m asl) (a) and the appearance of the disdrometer (b).

The disdrometer is a second-generation particle size and velocity (Parsivel) disdrometer, manufactured by OTT HydroMet, Germany. It is a laser-based disdrometer that can simultaneously detect the size and falling velocity of precipitation particles. The Parsivel transmits a parallel horizontal laser beam with a sampling area of 54 cm<sup>2</sup> (18-cm long, 3-cm wide), and a sampling time interval of 60 s. When particles pass through the laser beam, the received signals are attenuated and used to estimate the particle diameter; the duration can be utilized to detect the falling velocity. Raindrops larger than 1 mm are not spherical in Earth's atmosphere, so the estimation of the diameter is based on different axis ratio relationships. Specifically, for raindrops smaller than 1 mm and greater than 5 mm, the axis ratios are set to 1 and 0.7, respectively, and for raindrops between 1 and 5 mm, the axis ratio linearly varies from 1 to 0.7 [32,33]. After the diameter and falling velocity are measured, the raindrops are subdivided into 32 non-equidistant diameter classes, ranging from 0.062 to 24.5 mm and 32 non-equidistant velocity classes ranging from 0.05 to 20.8 m s<sup>-1</sup>. Detailed information about each diameter and velocity class can be seen in Yuter et al. (2006) [34].

The Parsivel has been widely used in measuring raindrop spectra during the last decade [18,19,34–48]. However, several shortcomings of the instrument also should be noticed. First, the raw measurements of drop size observed by Parsivel (as well as some other disdrometers, such as Joss-Waldvogel disdrometer, Precipitation Occurrence Sensor System, Precipitation Occurrence Sensor System, Thies disdrometer, Optical Spectro-pluviometer, etc.) are binned into fixed intervals based on the sensor accuracy [49–52]. This size binning can cause slight instabilities of the observed DSD and produce biases on its integral parameters and gamma parameters, moreover, the biases also closely related to the estimation methods [49]. Second, disdrometers typically use a short integration time (generally, the time does not exceed 1 min) to reduce the problems of DSD variability, whereas the short integration time will also cause sampling errors to measurements, which can become increasingly significant when the raindrop samples are reduced [53–55]. Third, studies confirmed that the Parsivel can underestimate/overestimate the number concentration of small/large raindrops [54,56–59]. Wen et al. (2017) found that this truncation problem has significantly solved for the second-generation Parsivel [56].

## 2.2. Data QC and Rainfall Physical Quantity Calculation

Apart from biases caused by the inherent limitations of Parsivel, several problematic data can be improved using the following QC technologies.

First, the data in the first two diameter classes were abandoned, due to their poor reliability of low signal-to-noise ratios, namely, the minimum detectable diameter of the raindrop was limited

to approximately 0.312 mm [33]. Second, any raindrop with a diameter larger than 8 mm was also eliminated, since it can mostly break up in the low level of Earth’s atmosphere. Third, considering the realistic instrument sensitivity, samples with a total drop number less than 10 or a rain rate smaller than 0.002 mm h<sup>-1</sup> were also removed [19]; otherwise, they were regarded as valid rain samples. Fourth, as proposed by Yuter et al. (2006) and Friedrich et al. (2013), any raindrop that possessed a normal falling velocity (or diameter) but with an unmatched (excessively larger or smaller) diameter (or falling velocity) was treated as unrealistic data. It can be produced when a large raindrop partially passes through or multiple raindrops parallelly pass through the laser beam; it can also be induced by a strong wind shear near the ground or splashing of raindrops on the instrument surface during heavy rainfalls [34,38]. This kind of problematic data was recognized by comparing the Parsivel-measured result with the theoretical diameter/falling velocity relationship shown in Equations (1) and (2) [60]. Therefore, any measured raindrop with a diameter greater than 1 mm was removed when it was ±60% outside of the theoretical value.

$$D = \frac{1}{0.6} \times \ln \frac{10.3}{9.65 - V_t / \delta(h)} \tag{1}$$

$$\delta(h) = 1 + 3.68 \times 10^{-5}h + 1.71 \times 10^{-9}h^2. \tag{2}$$

where  $D$  (mm) and  $V_t$  (m s<sup>-1</sup>) are the particle diameter and terminal falling velocity, respectively;  $h$  (m) is the sampling height above sea level; and  $\delta(h)$  is a correction factor.

The raindrop numbers in different diameter and velocity classes before and after QC for the entire data were counted and compared, as shown in Figure 2, to illustrate the QC effect. A small part of the raindrops that possessed an abnormal diameter (velocity), and some that were scattered or excessively large were removed. These unrealistic data accounted for only 1.76% of all raindrops, but they can occupy prominent proportions in the large-diameter and small-velocity classes. For the raindrops in classes with diameters from 2.75 to 7.5 mm, the problematic data accounted for 10.3% to 68%; for the raindrops in classes with velocities from 0.15 to 2.6 m s<sup>-1</sup>, the problematic data accounted for 34.87% to 94.59%.

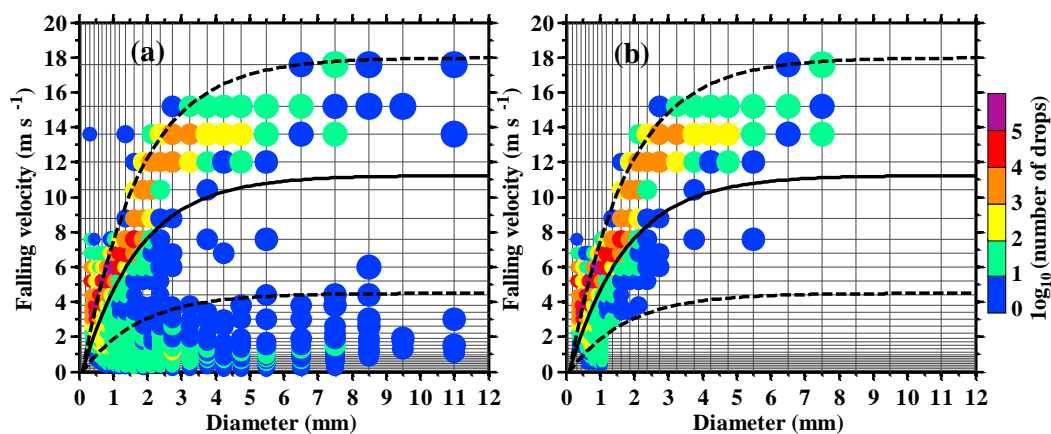


**Figure 2.** Raindrop numbers in the different diameter and falling-velocity classes before (a) and after (b) quality control (QC) for the entire dataset. The solid line represents the theoretical diameter/falling velocity relationship, as shown in Equations (1) and (2). The dashed line indicates the ±60% range of the relationship.

After QC, the DSD and its integral rainfall physical quantities, namely, including raindrop total number concentration  $N_T$  (m<sup>-3</sup>), rain rate  $R$  (mm h<sup>-1</sup>), rainwater content  $W$  (g m<sup>-3</sup>), reflectivity  $Z$  (mm<sup>6</sup> m<sup>-3</sup>), mass-weight mean diameter  $D_m$  (mm) and generalized intercept parameter  $N_w$  (m<sup>-3</sup> mm<sup>-1</sup>), can be further calculated as

$$N(D_i) = \sum_{j=1}^{32} \frac{n_{ij}}{A_i \cdot \Delta t \cdot V_j \cdot \Delta D_i} \tag{3}$$

$$N_T = \sum_{i=1}^{32} \sum_{j=1}^{32} \frac{n_{ij}}{A_i \cdot \Delta t \cdot V_j} \tag{4}$$

$$R = \frac{6\pi}{10^4} \sum_{i=1}^{32} \sum_{j=1}^{32} D_i^3 \frac{n_{ij}}{A_i \cdot \Delta t} \tag{5}$$

$$W = \frac{\pi}{6000} \cdot \rho_w \cdot \sum_{i=1}^{32} \sum_{j=1}^{32} D_i^3 \frac{n_{ij}}{A_i \cdot \Delta t \cdot V_j} \tag{6}$$

$$Z = \sum_{i=1}^{32} \sum_{j=1}^{32} D_i^6 \frac{n_{ij}}{A_i \cdot \Delta t \cdot V_j} \tag{7}$$

$$D_m = \frac{\sum_{i=1}^{32} N(D_i) D_i^4 \Delta D_i}{\sum_{i=1}^{32} N(D_i) D_i^3 \Delta D_i} \tag{8}$$

$$N_w = \frac{4^4}{\pi \rho_w} \left( \frac{10^3 W}{D_m^4} \right) \tag{9}$$

where  $i$  and  $j$  are the orders of the diameter and velocity classes, respectively;  $\Delta D_i$  (mm) is the interval of the diameter class;  $n_{ij}$  is the raindrop number within the diameter class  $i$  and velocity class  $j$ ;  $V_j$  ( $\text{mm s}^{-1}$ ) is the falling velocity of class  $j$ ;  $\Delta t$  (60 s) is the sampling time interval;  $A_i$  is the effective sampling area for  $i$ th diameter class; and  $\rho_w$  ( $1 \text{ g cm}^{-3}$ ) is the water density.  $N(D_i)$  ( $\text{m}^{-3} \text{ mm}^{-1}$ ) is the number concentration of raindrops per unit volume per millimeter. Note that the  $A_i$  of the Parsivel is associated with the raindrop size and can be estimated as  $180 \text{ mm} \times (30 \text{ mm} - 0.5D_i)$  [32,33].

The commonly used gamma distribution proposed by Ulbrich (1983) was implemented to fit the measured DSD, which can be expressed as follows [7],

$$N(D) = N_0 D^\mu \exp(-\Lambda D) \tag{10}$$

where  $N_0$  ( $\text{m}^{-3} \text{ mm}^{-1-\mu}$ ) is the intercept parameter related to the total number of raindrops.  $\mu$  is the shape parameter; a positive (negative)  $\mu$  indicates that the raindrop spectrum curve bends upwards (downwards).  $\Lambda$  ( $\text{mm}^{-1}$ ) is the slope parameter; a small (large)  $\Lambda$  can correspond to a flat (steep) spectrum. Several methods, such as the moment method (MM), the truncated moment method (TMM), the least square method (LS) and the maximum likelihood method (ML), have been used to estimate the DSD gamma parameters. Studies reported that the maximum likelihood method generally has a better performance than the others, and can be less sensitive to the DSD truncation problem and the short integration time of instrument [9,49,53,61–63]. Therefore, in this study, the maximum likelihood method was implemented to estimate the  $N_0$ ,  $\mu$ , and  $\Lambda$ .

### 2.3. Rain Type Classification

To study the DSD characteristics for the different rain types, the total dataset was further classified into two subsets, namely, stratiform and convective rains, based on the time series of the rain rate. Several classification schemes based on disdrometer measurements have been reported for the separation of convective versus stratiform rains, such as those of Tokay et al. (1996), Testud et al. (2001), Bringi et al. (2003) and Chen et al. (2013) [4,12,64,65]. In the current study, Bringi’s scheme was used to separate the two rain types. Specifically, set a moving window containing 11 rain samples in the time series. The standard deviation  $\sigma_R$  of rain rate of samples was calculated. If the  $\sigma_R$  was no more than  $1.5 \text{ mm h}^{-1}$ , the rain type of the center was determined as stratiform; otherwise, it was treated as convective. According to this classification principle, the window center was moved to the next sample every time until all samples in time series were identified. Note that the first five and last five

samples, which cannot be set to the window centers, were judged as the same rain type as the nearest window centers.

### 3. Results

In the following subsections, the DSD characteristics for different rain rates and types were investigated in detail. Subsequently, empirical relationships between gamma parameters and rainfall physical quantities for precipitation occurring on the eastern slope of the TP are proposed.

#### 3.1. DSD Characteristics for Different Rain Rates

DSD properties can vary largely under different rain rates [19,66]. Therefore, in this work, the total dataset was stratified into five rain-rate regimes, namely,  $R < 0.1 \text{ mm h}^{-1}$  (R1),  $0.1 \leq R < 1 \text{ mm h}^{-1}$  (R2),  $1 \leq R < 5 \text{ mm h}^{-1}$  (R3),  $5 \leq R < 10 \text{ mm h}^{-1}$  (R4) and  $R > 10 \text{ mm h}^{-1}$  (R5), to investigate the DSD characteristics for different rain rates. Figure 3 presents the accumulated rain amounts and durations for the five regimes. The results show that the ground rainfalls are dominated by light precipitation more than half of the time, with 65.15% of the total duration being produced by R1 and R2, whereas they account for only 12.51% of the total rain amount. The largest contributor to the total rain amount is R3, which accounts for 49.67% of the total rain amount and 31.14% of the total duration. For rainfalls with larger rain rates, R3 and R4 contribute only 3.71% of the total duration; nevertheless, they can produce 37.82% of the total rain amount.

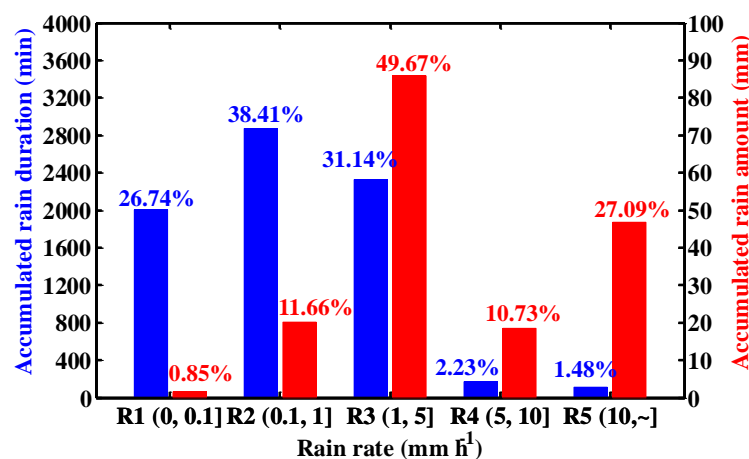


**Figure 3.** Accumulated durations (blue) and rain amounts (red) for the five rain-rate regimes. The percentages indicate the contributions of each rain-rate regime to the total duration and total rain amount.

The DSDs for the five rain-rate regimes were shown in Figure 4, in which the boxplots illustrate the raindrop number concentration in the different diameter classes. The results reveal that raindrop spectra can evidently change with the rain rates. Specifically, the raindrop spectra gradually become wider and flatter as the rain rate increases, owing to the contribution of large raindrops; the maximum measured diameters for R1 to R5 are 1.375, 2.75, 3.75, 4.25 and 7.5 mm. The raindrop number concentration in each diameter class also increases with the rain rate. The spectrum shapes for the five rain-rate regimes are both unimodal and generally obey the gamma distribution. The peaks of the medians both appear in the fifth diameter class, with a mean diameter of 0.562 mm. The number concentration of the raindrops in each diameter class can vary within three or more orders of magnitude, while raindrops between the 25th and 75th percentiles basically concentrate within one order of magnitude.

For a convenient comparison of the DSD characteristics under different rain rates, average raindrop spectra for R1 to R5 are superimposed on the same graph in Figure 5. The corresponding integral rainfall physical quantities derived from the average spectra and the fitted gamma parameters are listed in Table 1. The comparison shows that the total number concentration  $N_T$ , reflectivity  $Z$ , rainwater content  $W$  and mass-weighted mean diameter  $D_m$  increase with the rain rate. The largest generalized

intercept parameter  $N_W$  is found in R3. For the gamma parameters,  $N_0$ ,  $\mu$  and  $\Lambda$  decrease with an increased rain rate, corresponding to the widening and flattening of the raindrop spectra.

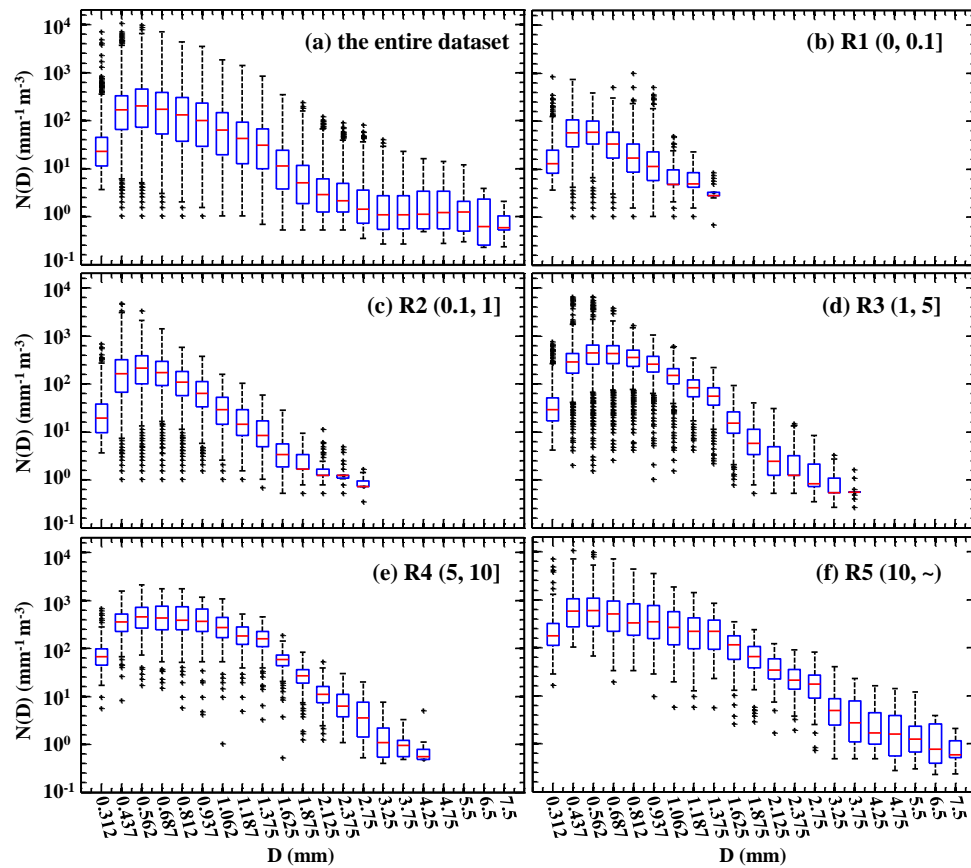


**Figure 4.** Boxplots of the raindrop size distributions (DSDs) for all datasets (a) and sub-datasets of five rain-rate regimes (b–f).  $D$  and  $N(D)$  are the raindrop diameter class and number concentration, respectively. For each boxplot, the bottom and top edges of the blue box indicate the 25th and 75th percentiles, respectively; the red central crossbar represents the median. The black dashed whiskers extend to the maximum and minimum of the data points, respectively, and the outliers are plotted individually using the “+” symbol.

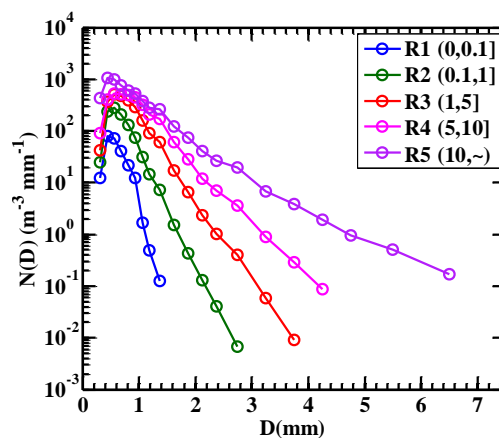


**Figure 5.** Averaged DSDs for the five indicated rainfall rates (R1–R5). The integral rainfall parameters derived from these averaged spectra are presented in Table 1. The circles represent the center of the Parsivel diameter classes.

**Table 1.** Integral rainfall physical quantities derived from the averaged DSDs and the fitted gamma distribution parameters for the five rain-rate regimes.

Class (mm <sup>-1</sup> )	$N_T$ (m <sup>-3</sup> )	Z (dBZ)	W (g m <sup>-3</sup> )	$D_m$ (mm)	$\log_{10}(N_W)$ (m <sup>-3</sup> mm <sup>-1</sup> )	$\log_{10}(N_0)$ (m <sup>-3</sup> mm <sup>-1-<math>\mu</math>)</sup>	$\mu$	$\Lambda$ (mm <sup>-1</sup> )
Total	175.24	30.18	0.0617	1.415	4.399	6.529	6.454	10.141
R1 (0, 0.1]	30.12	5.25	0.0038	0.723	4.009	11.088	12.951	24.364
R2 (0.1, 1]	127.84	17.24	0.0252	0.906	4.630	8.928	9.791	16.589
R3 (1, 5]	311.95	27.40	0.1086	1.177	4.868	6.858	6.817	10.203
R4 (5, 10]	436.34	35.26	0.2662	1.552	4.803	5.445	4.704	6.447
R5 (10, ~)	758.18	47.10	0.7594	2.541	4.472	4.541	2.526	3.995

### 3.2. DSD Characteristics for Different Rain Types

In this subsection, the DSD characteristics for stratiform and convective rains are analyzed and compared. During the observation period, there were 98 rainfall events, and 4599 DSD samples were obtained, of which 4217 (91.69%) were stratiform samples and 382 (8.31%) were convective samples, respectively. The accumulated rain amounts for the stratiform and convective samples are 66.37 and 47.45 mm, with mean rain rates of 0.94 and 7.45 mm h<sup>-1</sup>, respectively. Indicating that the rainfalls that happened in the Daocheng site are light stratiform rains most of the time. Meanwhile, although relatively sparse and short-lived, heavier convective rains can also produce a comparable rain amount.

The statistical DSDs for the stratiform and convective rains are shown in Figure 6. A comparison of the two sets of raindrop boxplots demonstrates that the convective rain has wider and flatter spectra than the stratiform rain, as a result of the contribution of larger raindrops; the maximum raindrop diameters for the convective and stratiform rains are 5.5 and 3.75 mm, respectively. The peaks of the medians for two rain types are both in the fifth diameter class, with a mean diameter of 0.562 mm. These comparison features of the two rain types are quite similar to the comparison results of the raindrop spectra between the low-rain-rate regime and the high-rain-rate regime, as concluded in Section 3.1.

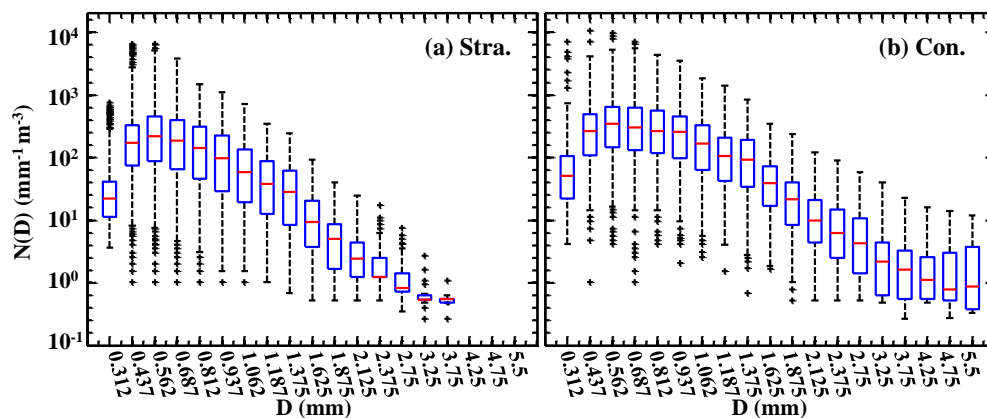


**Figure 6.** Boxplots of the DSDs for the stratiform (a) and convective (b) samples. D and N(D) are the raindrop diameter class and number concentration, respectively. The meaning of the boxplot is described in the caption of Figure 4.

Figure 7 presents the probability distributions of values of DSD-derived R, Z, W,  $N_T$ ,  $D_m$ ,  $N_W$ ,  $N_0$ ,  $\mu$  and  $\Lambda$  to discern the differences in the rainfall physical quantities and gamma parameters of two rain types. Their corresponding 5th, 25th, 75th, 95th percentiles, medians and averages are also summarized in Table 2. It can be found that, generally, the stratiform rain has smaller values of R, Z, W,  $N_T$  and  $D_m$ , but larger values of  $N_0$ ,  $\mu$  and  $\Lambda$  than the convective rain. The  $N_W$ s of two rain types are very close.

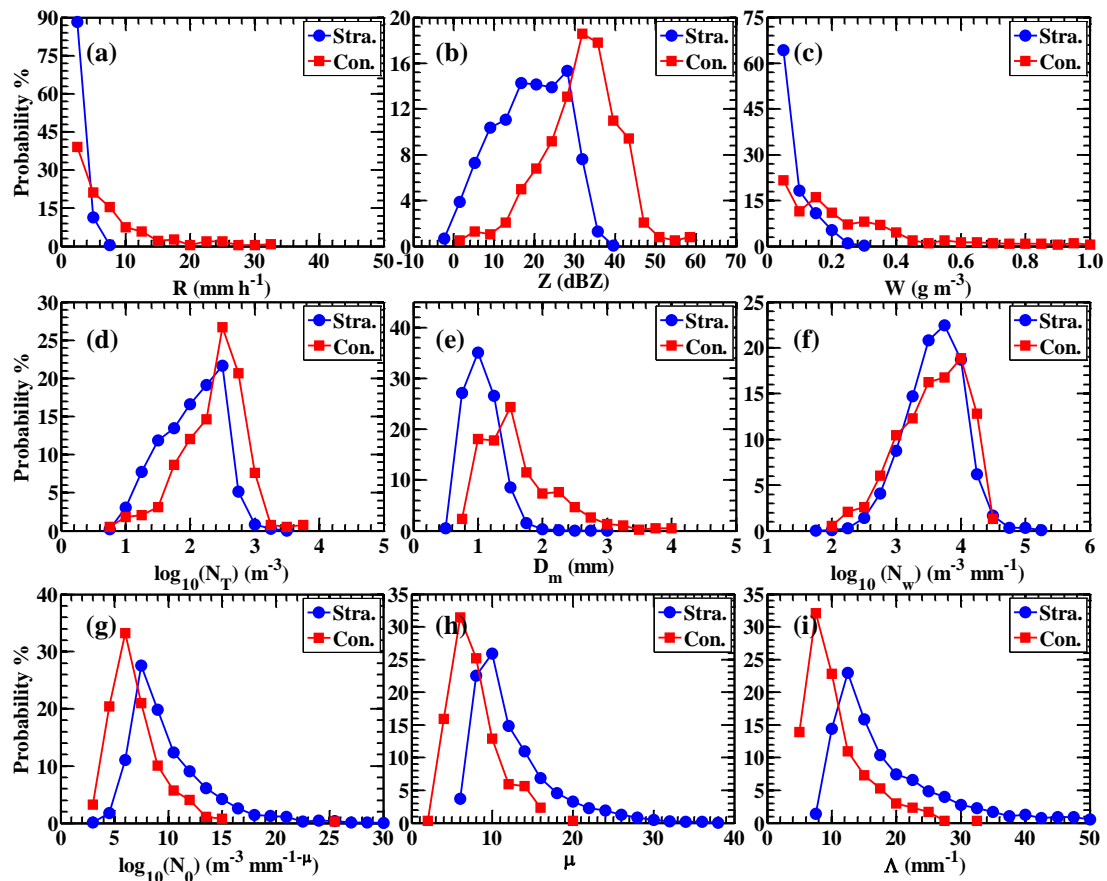


**Figure 7.** Probability distributions of the integral rainfall physical quantities and gamma distribution parameters. (a–i) are the rain rate ( $R$ ), reflectivity ( $Z$ ), rainwater content ( $W$ ), total number concentration ( $N_T$ ), mass-weighted mean diameter ( $D_m$ ), generalized intercept parameter ( $N_w$ ), gamma intercept parameter ( $N_0$ ), gamma shape parameter ( $\mu$ ) and gamma slope parameter ( $\Lambda$ ).

**Table 2.** The 5th, 25th, 75th, 95th percentiles, medians and averages of integral rainfall physical quantities and gamma distribution parameters for two rain types.

Rainfall Quantities and Gamma Parameters	Rain Types	5th	25th	Median	Average	75th	95th
$R$ ( $\text{mm h}^{-1}$ )	Stra.	0.026	0.121	0.454	0.944	1.432	3.261
	Con.	0.168	1.314	3.818	7.453	7.706	23.437
$W$ ( $\text{g m}^{-3}$ )	Stra.	0.002	0.008	0.028	0.049	0.074	0.159
	Con.	0.009	0.066	0.154	0.265	0.311	0.786
$Z$ (dBZ)	Stra.	0.286	9.246	16.559	16.115	23.804	29.281
	Con.	12.005	23.767	30.767	29.585	35.916	43.002
$D_m$ (mm)	Stra.	0.575	0.734	0.899	0.932	1.099	1.377
	Con.	0.803	1.073	1.379	1.496	1.812	2.666
$\log_{10}N_T$ ( $\text{m}^{-3}$ )	Stra.	1.201	1.664	2.081	2.023	2.407	2.656
	Con.	1.408	2.062	2.446	2.356	2.683	2.992
$\log_{10}N_w$ ( $\text{m}^{-3} \text{mm}^{-1}$ )	Stra.	2.717	3.193	3.498	3.467	3.774	4.111
	Con.	2.481	3.097	3.494	3.437	3.874	4.131
$\log_{10}N_0$ ( $\text{m}^{-3} \text{mm}^{-1-\mu}$ )	Stra.	5.301	6.671	8.146	9.236	10.878	16.844
	Con.	3.184	4.572	5.663	6.123	7.084	10.859
$\mu$	Stra.	5.055	7.009	9.164	10.646	12.959	21.147
	Con.	1.999	3.429	5.271	6.009	7.775	12.837
$\Lambda$ ( $\text{mm}^{-1}$ )	Stra.	7.173	10.132	13.847	16.453	20.692	34.061
	Con.	2.663	4.805	7.027	8.581	11.018	20.015

The average DSDs and gamma distribution curves fitted by the ML for two rain types are further presented in Figure 8. Table 3 lists the corresponding rainfall physical quantities and gamma parameters for the average spectra. The results show that the average DSD of convective rain is broader and flatter than that of the stratiform rain. The former also possess higher number concentrations than the latter at each diameter class. For comparison, fitted results using the MM are also superimposed on the figure. Comparisons indicate that the MM significantly underestimates the raindrop number concentration of small raindrops, and the biases of ML are much smaller. On the contrary, for medium raindrops, the ML overestimates the results, and the MM can perform better. The correlation coefficients between the observed and fitted DSDs of the stratiform rain for the ML and MM are 0.9426 and 0.9575, respectively, and the counterparts of the convective rain are 0.9132 and 0.9574, respectively. We also use the Kolmogorov-Smirnov (KS) test to verify the fitting methods. The results show that two methods both can pass the verification. The KS p-values of ML and MM for the stratiform rain are both 0.9123, and they are 0.3841 and 0.9123, respectively, for the convective rain. Overall, the gamma distribution can adequately describe the observed rain spectra, and the fitted results for the average DSDs of two rain types can be expressed as

$$N(D) = 5.582 \times 10^5 D^{5.282} \exp(-8.167D), \text{ stratiform rain} \tag{11}$$

$$N(D) = 1.872 \times 10^4 D^{2.622} \exp(-3.947), \text{ convective rain} \tag{12}$$

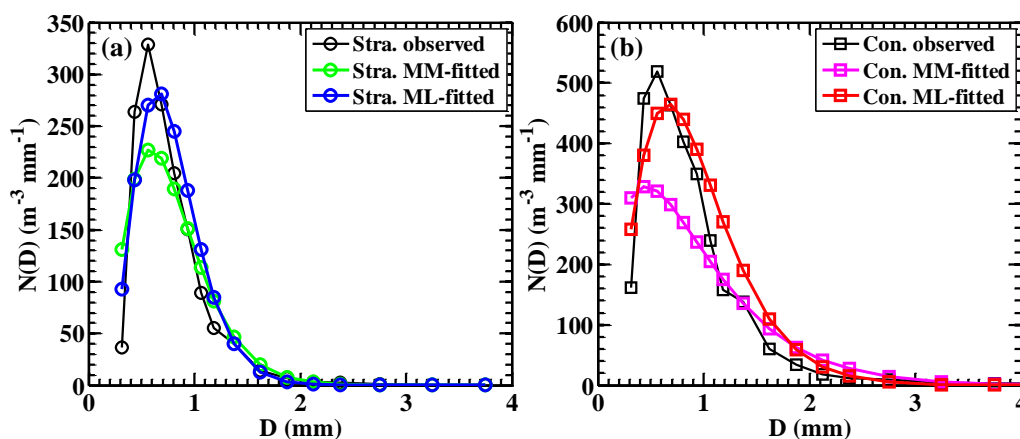


**Figure 8.** Average DSDs for the stratiform (a) and convective (b) rains, and fitted results using the maximum likelihood method (ML) and moment method (MM).

**Table 3.** Integral rainfall physical quantities and gamma parameters derived from the averaged DSDs for the stratiform and convective rains, using the maximum likelihood method.

Rain Types	R (mm h <sup>-1</sup> )	N <sub>T</sub> (m <sup>-3</sup> )	Z (dBZ)	W (g m <sup>-3</sup> )	D <sub>m</sub> (mm)	log <sub>10</sub> (N <sub>W</sub> ) (m <sup>-3</sup> mm <sup>-1</sup> )	log <sub>10</sub> (N <sub>0</sub> ) (m <sup>-3</sup> mm <sup>-1-μ</sup> )	μ	Λ (mm <sup>-1</sup> )
Stra.	0.85	172.73	22.98	0.0490	1.094	4.649	5.746	5.282	8.167
Con.	6.21	390.07	39.01	0.2573	1.911	4.475	4.272	2.622	3.947

### 3.3. Relationship of μ – Λ

The gamma parameters are not mutually independent. The relations between μ and N<sub>0</sub>/Λ can provide useful information reflecting the behavior of the rain spectra, and facilitate their application in other areas. Empirical relationships between the gamma distribution parameters have been presented by researchers. Ulbrich and Atlas (1998) found that the μ – N<sub>0</sub> relationship can be expressed by an exponential equation [67]. Brandes et al. (2003) proposed a second-order polynomial μ – Λ relationship, which can be written as [68]

$$\Lambda = 0.0365\mu^2 + 0.735\mu + 1.935 \tag{13}$$

Many other scientists have reported similar equations, but their studies showed different coefficients; such variation can be directly related to the studied geographical locations and climatological regimes [5,9,11,12,19,35,41]. Some criteria are used before data fitting to obtain more reliable relations of  $\mu - N_0$  and  $\mu - \Lambda$ ; for example, in the works of Zhang et al. (2003), Chen et al. (2017), Zhang et al. (2019) and Huo et al. (2019), a threshold of raindrop total number was set to 1000 for selecting fitted samples. They considered that the fitted gamma parameters of DSDs with drop counts less than this threshold may be less representative, because of the limitation of fitting approaches [3,19,35,41]. Chen et al. (2017) set the threshold to 300 since the raindrop number concentration over the TP is relatively lower [19].

The relationships of  $\mu - N_0$  and  $\mu - \Lambda$  are also fitted in this study. The results show that there is a good correlation between the  $\mu$  and  $\Lambda$  with a certain quadratic relationship, however, the relation between  $\mu$  and  $N_0$  is unapparent. Figure 9 shows the scatterplots of the  $\mu$  and  $\Lambda$ . The gray plots represent the entire data, and the black plots are samples after selection by a threshold of total raindrop number proposed by Chen et al. (2017). The black plots can distribute more concentratedly samples, and have higher representativeness than the entire data. The fitting result of the black plots exhibits a confidential  $\mu - \Lambda$  relationship. The correlation coefficient between the observed and fitted  $\Lambda$  is 0.9522, and the fitted result can pass the KS-test with a high p-value of 0.9911. The  $\mu - \Lambda$  relationship can be expresses as

$$\Lambda = 0.0302\mu^2 + 1.139\mu + 0.724 \tag{14}$$

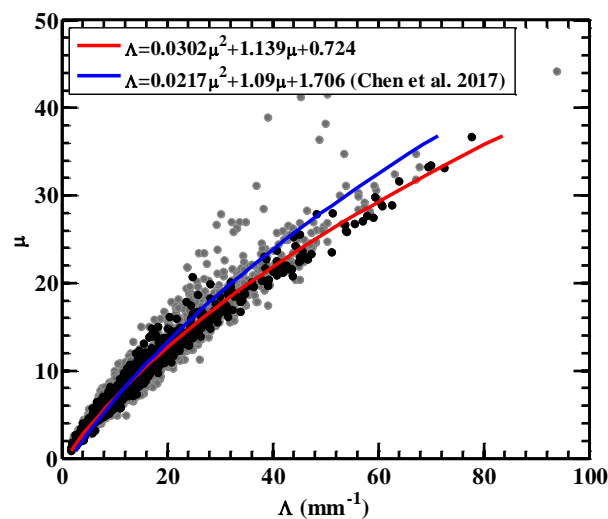


**Figure 9.** Scatterplots of the gamma parameters of  $\Lambda$  and  $\mu$ . The gray and black points are from the entire data and the filtered data with drop counts greater than 300, respectively. The red line represents our relationship, the blue line is the relationship for rainfalls in the mid-TP proposed by Chen et al. (2017) [19].

The relationship of  $\mu - \Lambda$  for DSDs observed in the mid-TP that were proposed by Chen et al. (2017) is compared (the blue solid line). Our relationship is quite consistent with Chen’s result, but our formula can produce a larger  $\Lambda$  under the same  $\mu$ .

### 3.4. Relationships of $D_m - R$ and $N_w - R$

The  $D_m$  and  $N_w$  are independent quantities that can synthetically represent the size and number concentration of the rain spectrum. Tables 1 and 3 preliminarily indicate that  $D_m$  and  $N_w$  can remarkably change with the rain rate  $R$  and show differences with respect to rain types. Therefore, relationships between  $D_m$  ( $N_w$ ) and  $R$  are further discussed in this subsection. In many studies, a power-law equation, namely,  $D_m/N_w = AR^B$ , was used to formulize the  $D_m - R$  and  $N_w - R$  relationships, but with different coefficients of  $A$  and  $B$ , due to the different geographical locations [19,35,69,70]. In this study, we also use the power-law formula to fit the relationships of  $D_m - R$  and  $N_w - R$ .

Figure 10 presents the scatterplots of  $R$  versus  $D_m/N_w$  and fitted curves for two rain types. The  $D_m$  and  $N_w$  for samples can both increase along with  $R$ , while they exhibit different incremental features for two rain types. Specifically, the stratiform rain has larger increments of  $D_m$  and  $N_w$  at small  $R$  values. As  $R$  increases, the  $D_m$  and  $N_w$  of can more easily tend to be stable than those of the convective rain. This difference can imply that the raindrop formation and growth can be efficient under a small rain rate for the stratiform rain. In contrast, as the rain rate increase, physical processes can gradually tend to an equilibrium to yield raindrop spectra with small increments in both size and concentration. The convective rain can continually produce larger raindrops, along with an increase in the rain rate, indicating that the raindrop growth process can remain efficient, as a result of abundant water vapor and strong updrafts.

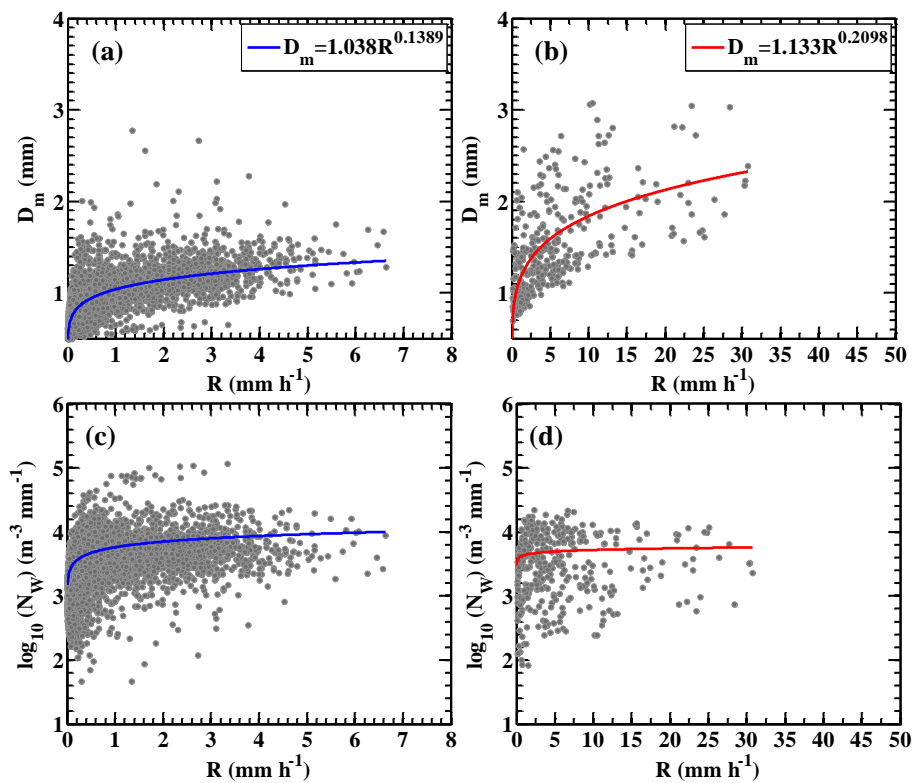


**Figure 10.** Scatterplots of the mass-weight mean diameter  $D_m$  and generalized intercept parameter  $N_w$  versus the rain rate  $R$ . (a)  $D_m$  versus  $R$  for the stratiform rain, (b)  $D_m$  versus  $R$  for the convective rain, (c)  $N_w$  versus  $R$  for the stratiform rain, (d)  $N_w$  versus  $R$  for the convective rain. The blue and red lines are the results for the stratiform and convective rains fitted using the linear least squares method.

We use the KS test to verify the fitted relationships of  $D_m - R$  and  $N_w - R$ . The results show that the fitting of  $D_m - R$  relationship is basically confidential, while the correlation between  $N_w$  and  $R$  for both two rain types is unapparent. The fitted  $D_m - R$  relationships for two rain types are given as

$$D_m = 1.038R^{0.1389}, \text{ stratiform rain} \tag{15}$$

$$D_m = 1.133R^{0.2098}, \text{ convective rain} \tag{16}$$

### 3.5. Relationship of $Z - R$

The relationship between  $Z$  and  $R$  has a substantial significance for improving radar QPE. Many studies have investigated the power-law relationship of  $Z = AR^b$  for stratiform and convective rains using disdrometers, and proposed specific coefficients of  $A$  and  $b$  for different geographical locations [30,41,65,71–76]. Typically, the relationship of  $Z = 300R^{1.4}$  for convective rains that was

proposed by Fulton et al. (1998) is used in the Next-Generation Weather Radar of the United States [73]. The relationship of  $Z = 200R^{1.6}$  presented by Marshall and Palmer (1963) has also been commonly applied to mid-latitude areas for stratiform rains [72]. Herein, we also investigate the relationships for the different rain types on the eastern slope of the TP. Figure 11 shows the statistical results of  $Z$  versus  $R$  and the fitted relationships. The scatterplots of the samples indicate that  $Z$  and  $R$  well obey the power-law relationships for both rains. The correlation coefficients between the fitted and observed results for stratiform and convective rains are 0.8729 and 0.968. The fitted relationships of  $Z - R$  can pass the KS test, and they can be expressed as

$$Z = 149R^{1.489}, \text{ stratiform rain} \quad (17)$$

$$Z = 107.7R^{1.79}, \text{ convective rain} \quad (18)$$

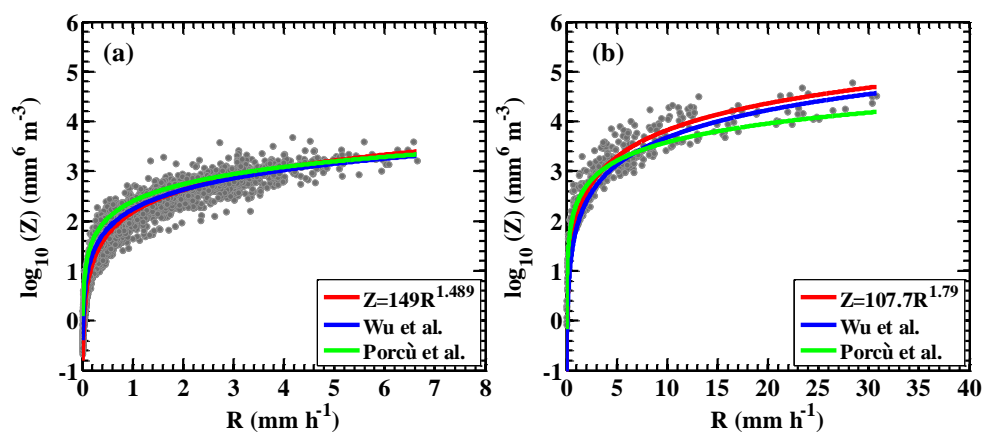


**Figure 11.** Scatterplots of  $Z$  versus  $R$  for the stratiform (a) and convective (b) rains. The blue and red lines are the fitted relationships. The green lines are the results from Wu et al. (2017) [30] and Porcù et al. (2014) [31] for the mid- and southern TP.

#### 4. Discussion

In this section, we compare our results regarding DSD characteristics with those obtained in other areas of China. Biases of the ML method and the proposed  $Z - R$  relationship are also discussed.

##### 4.1. Comparison of DSD Characteristics

(1) Average DSDs: average DSDs of the stratiform and convective rains observed in our area are compared with results obtained in the mid-TP, East China and South China. Figure 12 shows that both DSDs of two rain types on the eastern slope of TP are different from those in the other areas. For the stratiform rain, spectrum in our area is narrower than that in other areas. The number concentrations of small raindrops ( $<1.4$  mm) are closest to those in South China, followed by East China, and they are apparently higher than those in the mid-TP. However, for larger raindrops, their number concentrations in our area are smaller than those in the other three regions. For the convective rain, the DSD in our area is closest to that in the mid-TP. Their differences are also significant. Convective DSDs in our area generally produce higher number concentrations of small and medium raindrops ( $<2$  mm) than those in the mid-TP. On the contrary, the number concentrations of larger raindrops of the former are lower than those of the latter.

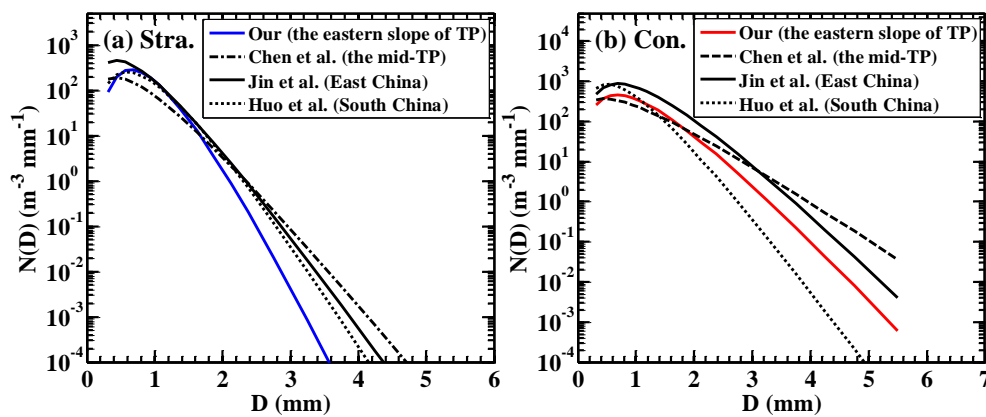


**Figure 12.** Average DSDs of the stratiform (a) and convective (b) rains observed in our area and other areas of China (the mid-TP: Chen et al. 2017 [19]; East China: Jin et al. 2015 [70]; South China: Huo et al. 2019 [35]).

(2)  $D_m - \log_{10}(N_w)$  domain: Figure 13 shows the scatterplots of  $D_m$  versus  $\log_{10}(N_w)$  for two rain types observed in our area. The gray points represent all samples. The red crosses represent the averages of  $D_m - \log_{10}(N_w)$ . The results show that the convective rain has a larger mean  $D_m$  and a comparable  $N_w$  compared with those of the stratiform rain. The averages of  $D_m - \log_{10}(N_w)$  for the stratiform and convective rains are 0.932–3.468 and 1.5–3.437, respectively. The black stars, blue squares, green circles and purple pluses are averages observed in other four climatic regimes in China. Comparisons of the five pairs of averages indicates that the  $D_m - \log_{10}(N_w)$  for two rain types observed in our area are both different from those observed in other areas. For the stratiform rain, the mean  $D_m$  of our area is the same as that of the mid-TP, but smaller than those of non-plateau areas. The mean  $N_w$  of our area can be larger than that of North China, but smaller than those of other three areas. For the convective rain, the mean  $D_m$  of our area is slightly larger than that of North China but smaller than other areas. The mean convective  $N_w$  of our area is larger than that of North China, but smaller than those of other areas.

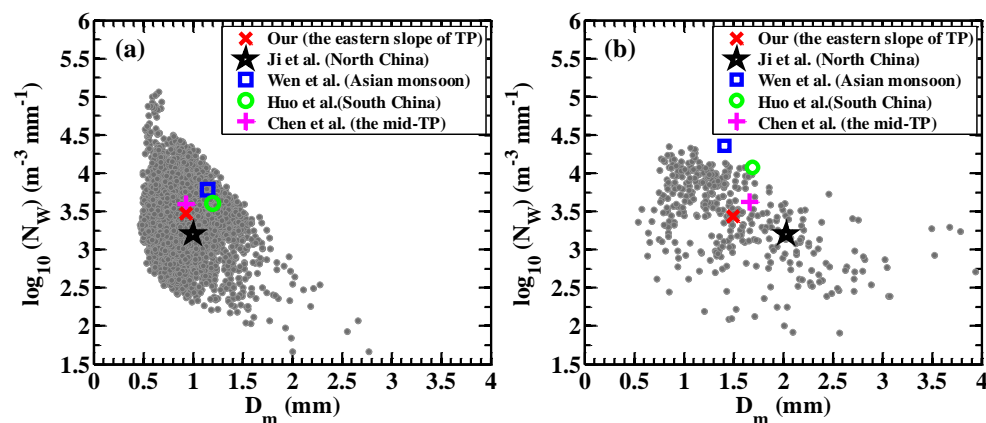


**Figure 13.** Scatterplots of  $D_m$  versus  $\log_{10}(N_w)$  for the stratiform (a) and convective (b) rains. The gray points represent all samples. The red cross represents the average  $D_m - \log_{10}(N_w)$  obtained in our area. The black stars, blue squares, green circles and purple pluses are the results obtained in other areas of China (the mid-TP: Chen et al. 2017 [19]; North China: Ji et al. 2020 [76]; South China: Huo et al. 2019 [35]; Asian summer monsoon: Wen et al 2016 [14]).

(3)  $Z - R$  relationship: for comparison, the  $Z - R$  relationships for two rain types in the mid- and southern TP proposed by Wu et al. (2017) and Porcù et al. (2014) are also drawn in Figure 11. Comparisons show that the stratiform  $Z - R$  relationship of our area is very close to the other results. For a 30-dBZ ( $10^3 \text{ mm}^6 \text{ m}^{-3}$ )  $Z, R$  values for our area, the mid-TP, and the southern TP are 3.38, 3.59

and  $3.85 \text{ mm h}^{-1}$ . For the convective rain, the relationship of our area is different from those of the other two areas, but relatively closer to that of the mid-TP. For a 40-dBZ ( $10^4 \text{ mm}^6 \text{ m}^{-3}$ ) Z, R values for our area, the mid-TP, and the southern TP are 12.57, 15.07 and  $21.65 \text{ mm h}^{-1}$ . Overall, the Z – R relationship of convective rain has a smaller A, but a larger b than the stratiform rain.

4.2. Biases of ML Method and Z – R Relationship

To evaluate the performance of ML method in application to DSD fitting, the relative error (RE) of the gamma-fitted compared to the observed DSDs, and the derived integral rainfall quantities are further calculated. Figure 14a,b shows boxplots of REs of the raindrop number concentration in different diameter classes for two rain types. The RE of  $N_T$ , Z,  $D_m$ , R, W, and  $N_w$  are depicted in Figure 14c,d, respectively. The results show that most of the gamma-fitted DSDs overestimate the number concentration of small raindrops at 0.312 mm diameter class for both of the two rain types; whereas, the biases for raindrops at larger diameter classes rapidly decrease. For the stratiform rain, the REs ranging from 0.437- to 1.375 mm are relatively smaller than other classes; their 25th–75th percentiles and averages of REs are both within 50%; for the larger raindrops at 1.625- to 3.25 mm classes, the underestimation becomes remarkable. For the convective rain, the overestimation at 0.312 mm class is smaller compared to the stratiform rain; the 25th–75th and averages of REs of a wider scope of diameter classes (0.437 to 2.375 mm classes) are within 50%.

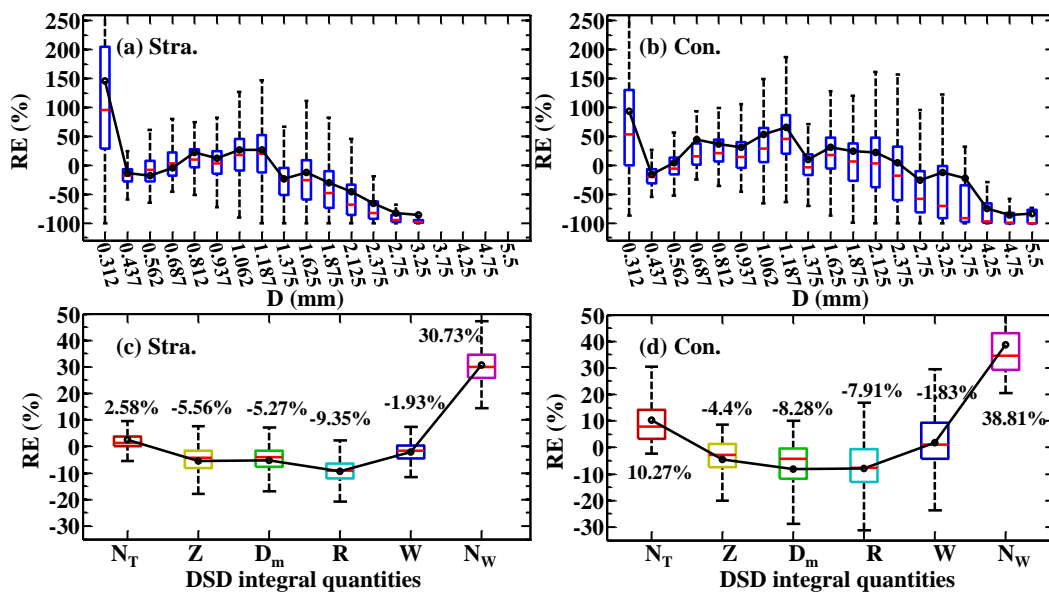


**Figure 14.** Relative errors (REs) of the gamma-fitted results. (a) and (b) are RE boxplots of raindrop number concentration in different diameter classes for two rain types. (c) and (d) are RE boxplots of the DSD-derived rainfall quantities [raindrop total number concentration  $N_T$  ( $\text{m}^{-3}$ ), reflectivity Z (dBZ), mass-weighted mean diameter  $D_m$  (mm), rain rate R ( $\text{mm h}^{-1}$ ), rainwater content W ( $\text{g m}^{-3}$ ), generalized intercept parameter  $\log_{10}(N_w)$  ( $\text{m}^{-3} \text{ mm}^{-1}$ )] for two rain types. The black lines with circles in subgraphs represent the averages.

For the six DSD-derived quantities, gamma-fitted DSDs underestimate the Z,  $D_m$ , R and W, but overestimate the  $N_T$  and  $N_w$  for both rain types. The REs of  $N_w$  are larger than the other quantities, indicating that the gamma function fitted by ML method can produce steeper raindrop spectra than the reality.

The RE of relationship-derived compared to the observed rain rates (Rs) are also calculated, to estimate the biases of the proposed Z – R relationship in the application to rainfall quantitative estimation. Figure 15 shows the boxplots of RE of the rain rate in different regimes for two rain types. Note that the R regimes for two rain types are assigned to be different because of their different value

ranges. Obviously, with the increase of  $R$ , the REs of both two rain types are decreased. The biases in the first two  $R$  regimes ( $R \leq 1 \text{ mm h}^{-1}$ ) are much smaller than those in the posterior  $R$  regimes. For the rainfalls with rain rates greater than  $1 \text{ mm h}^{-1}$ , the boxplots of RE of stratiform rain possess 25th–75th percentiles and averages within  $-27\%$ – $18\%$ , while  $-45\%$ – $30\%$  can be found for the convective rain type. Overall, the proposed  $Z - R$  relationship can produce smaller biases for the stratiform rain than that for the convective rain, and it is more accurate for the rainfalls with a rain rate greater than  $1 \text{ mm h}^{-1}$ .

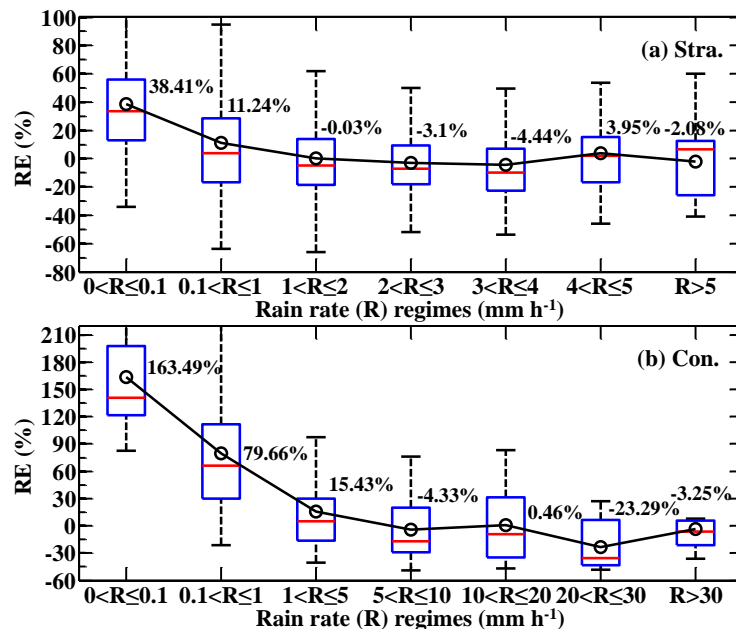


**Figure 15.** Relative errors (REs) of the relationship-derived compared to the observed rain rates ( $R_s$ ) in different regimes for stratiform (a) and convective (b) rains. The black lines with circles and black-font values both represent the averages.

## 5. Conclusions

The precipitation microphysics in different regions of the TP can be significantly different, because of the enormous and complex terrains and different climates. However, only limited observations and studies have reported the rainfall microphysics in the mid-TP. In this paper, we present a comprehensive study of characteristics of DSDs for rainfalls that happened on the eastern slope of TP. The main findings can be summarized as follows.

(1) As many studies revealed, DSD differences between the stratiform and convective rains and under different  $R$  regimes are also apparent on the eastern slope of TP. The stratiform rain contributes to more rain duration and amount compared with the convective rain. Whereas, it has much smaller  $R$ ,  $Z$ ,  $W$ ,  $D_m$  and  $N_T$ , but larger  $N_0$ ,  $\mu$  and  $\Lambda$ , and produces narrower and steeper rain spectra than the convective rain. As  $R$  increase, both DSDs of two rain types become wider, corresponding to occurrences of larger raindrops and higher concentrations.

(2) The DSD characteristics on the eastern slope of TP can be different from those in other areas. The stratiform DSD in this area is narrower than in non-plateau regions, because of the smaller rainfall intensity. The convective DSD in this area also can be narrower than that in East China, but broader than that in South China. The differences of rain spectra between this area and the mid-TP are also significant. For stratiform spectra in this area, number concentrations of raindrops (within  $0.437$ – $1.625 \text{ mm}$ ) are higher than those in the mid-TP. On the contrary, for raindrops smaller than  $0.437 \text{ mm}$  and larger than  $1.635 \text{ mm}$ , the former has lower number concentrations than the latter. The differences of the convective spectra between two areas are similar to those of the stratiform spectra.

(3) The confidential relationships of  $\mu - \Lambda$  and  $Z - R$  for rainfalls in this area are proposed with KS test. Comparisons of these relationships with the counterparts in other areas indicate that, rain spectra

in this area can produce a larger  $\Lambda$  under the same  $\mu$  than rain spectra in the mid-TP. The  $Z - R$  relationship of stratiform rain is very close to that in the mid-TP, whereas, the counterpart of convective rain can produce a smaller  $R$  under the same  $Z$ .

(4) Comparisons of the  $D_m$  and  $N_W$  observed in this area with those obtained in other areas (North China, South China, Asian summer monsoon area and the mid-TP) show that the  $D_m$  and  $N_W$  of this area are closest to those in the area of the mid-TP. However, the former  $N_W$  of the stratiform rain is slightly smaller than the latter with the same  $D_m$ . The former  $D_m$  and  $N_W$  of the convective rain are both smaller than those of the latter.

(5) Estimation of the gamma fitting using ML method indicated that the gamma fitted DSDs could overestimate (underestimate) the number concentration of small (large) raindrops. The bias of  $Z - R$  relationship in application to QPE can decrease with the increase of  $R$ . Overall, for both of the two rain types, their relationships can possess acceptable accuracy when  $R$  exceeds  $1 \text{ mm h}^{-1}$ .

**Author Contributions:** Conceptualization, J.Z.; methodology, J.Z.; software, Y.W.; validation, Z.C., B.W.; formal analysis, J.Z.; investigation, Y.W.; resources, J.Z.; data curation, J.Z.; writing—original draft preparation, J.Z.; writing—review and editing, J.Z.; visualization, Y.W.; supervision, Z.C.; project administration, B.W.; funding acquisition, Z.C. All authors have read and agreed to the published version of the manuscript.

**Funding:** This research was funded by the science project of “Research on Forecast and Early Warning of Icing on Overhead Transmission Lines in Micro-topographic Areas” (Grant no. 521999180006).

**Acknowledgments:** We want to thank the editor and anonymous reviewers for their valuable suggestions and comments for improving this manuscript.

**Conflicts of Interest:** The authors declare no conflict of interest.

## References

1. Wu, G.; Zhang, Y. Tibetan plateau forcing and the timing of the monsoon onset over South Asia and the South China Sea. *Mon. Weather Rev.* **1998**, *126*, 913–927. [[CrossRef](#)]
2. Zhao, P.; Xu, X.D.; Chen, F.; Guo, X.L.; Zheng, X.D.; Liu, L.P.; Hong, Y.; Li, Y.Q.; La, Z.; Peng, H.; et al. The third atmospheric scientific experiment for understanding the earth-atmosphere coupled system over the tibetan plateau and its effects. *Bull. Am. Meteorol. Soc.* **2018**, *99*, 757–776. [[CrossRef](#)]
3. Zhang, G.; Vivekanandan, J.; Brandes, E.A.; Meneghini, R.; Kozu, T. The shape–slope relation in observed gamma raindrop size distributions: Statistical error or useful information? *J. Atmos. Ocean. Technol.* **2003**, *20*, 1106–1119. [[CrossRef](#)]
4. Bringi, V.N.; Chandrasekar, V.; Hubbert, J.; Gorgucci, E.; Randeu, W.L.; Schoenhuber, M. Raindrop size distribution in different climatic regimes from disdrometer and dual-polarized radar analysis. *J. Atmos. Sci.* **2003**, *60*, 354–365. [[CrossRef](#)]
5. Cao, Q.; Zhang, G.; Brandes, E.; Schuur, T.; Ryzhkov, A.; Ikeda, K. Analysis of video disdrometer and polarimetric radar data to characterize rain microphysics in Oklahoma. *J. Appl. Meteorol. Clim.* **2008**, *47*, 2238–2255. [[CrossRef](#)]
6. Rosenfeld, D.; Ulbrich, C.W. Cloud microphysical properties, processes, and rain fall estimation opportunities. *Meteorol. Monogr.* **2003**, *30*, 237–258. [[CrossRef](#)]
7. Ulbrich, C.W. Natural variations in the analytical form of the raindrop size distribution. *J. Clim. Appl. Meteorol.* **1983**, *22*, 1764–1775. [[CrossRef](#)]
8. Ulbrich, C.W.; Atlas, D. Microphysics of raindrop size spectra: Tropical continental and maritime storms. *J. Appl. Meteorol. Clim.* **2007**, *46*, 1777–1791. [[CrossRef](#)]
9. Brawn, D.; Upton, G. Estimation of an atmospheric gamma drop size distribution using disdrometer data. *Atmos. Res.* **2008**, *87*, 66–79. [[CrossRef](#)]
10. Thurai, M.; Bringi, V.N.; May, P.T. CPOL radar-derived drop size distribution statistics of stratiform and convective rain for two regimes in Darwin, Australia. *J. Atmos. Ocean. Technol.* **2010**, *27*, 932–942. [[CrossRef](#)]
11. Kumar, L.S.; Lee, Y.H.; Ong, J.T. Two-parameter gamma drop size distribution models for Singapore. *IEEE Trans. Geosci. Remote Sens.* **2011**, *49*, 3371–3380. [[CrossRef](#)]
12. Chen, B.; Yang, J.; Pu, J. Statistical characteristics of raindrop size distribution in the Meiyu season observed in eastern China. *J. Meteorol. Soc. Jpn.* **2013**, *91*, 215–227. [[CrossRef](#)]

13. Friedrich, K.; Kalina, E.A.; Masters, F.J.; Lopez, C.R. Drop-size distributions in thunderstorms measured by optical disdrometers during VORTEX2. *Mon. Weather Rev.* **2013**, *141*, 1182–1203. [[CrossRef](#)]
14. Wen, L.; Zhao, K.; Zhang, G.; Xue, M.; Zhou, B.; Liu, S.; Chen, X. Statistical characteristics of raindrop size distributions observed in East China during the Asian summer monsoon season using 2-D video disdrometer and micro rain radar data. *J. Geophys. Res. Atmos.* **2016**, *121*, 2265–2282. [[CrossRef](#)]
15. Uijlenhoet, R.; Smith, J.A.; Steiner, M. The microphysical structure of extreme precipitation as inferred from ground-based raindrop spectra. *J. Atmos. Sci.* **2003**, *60*, 1220–1238. [[CrossRef](#)]
16. Barthes, L.; Mallet, C. Vertical evolution of raindrop size distribution: Impact on the shape of the DSD. *Atmos. Res.* **2013**, *119*, 13–22. [[CrossRef](#)]
17. Kirankumar, N.V.P.; Narayana, R.T.; Radhakrishna, B.; Rao, D.N. Statistical characteristics of raindrop size distribution in southwest monsoon season. *J. Appl. Meteorol. Clim.* **2008**, *47*, 576–590. [[CrossRef](#)]
18. Niu, S.; Jia, X.; Sang, J.; Liu, X.; Lu, C.; Liu, Y. Distributions of raindrop sizes and fall velocities in a semiarid plateau climate: Convective versus stratiform rains. *J. Appl. Meteorol. Clim.* **2010**, *49*, 632–645. [[CrossRef](#)]
19. Chen, B.; Hu, Z.; Liu, L.; Zhang, G. Raindrop size distribution measurements at 4,500 m on the Tibetan Plateau during TIPEX-III. *J. Geophys. Res. Atmos.* **2017**, *122*, 11092–11106. [[CrossRef](#)]
20. Geoffroy, O.; Siebesma, A.P.; Burnet, F. Characteristics of the raindrop distributions in RICO shallow cumulus. *Atmos. Chem. Phys.* **2014**, *14*, 10897–10909. [[CrossRef](#)]
21. Li, H.; Yin, Y.; Shan, Y.P.; Jin, Q. Statistical characteristics of raindrop size distribution for stratiform and convective precipitation at different altitudes in Mt. Huangshan. *Chin. J. Atmos. Sci.* **2018**, *42*, 268–280. [[CrossRef](#)]
22. Bao, X.; Wu, L.; Tang, B.; Ma, L.; Wu, D.; Tang, J.; Chen, H.; Wu, L. Variable Raindrop Size Distributions in Different Rainbands Associated with Typhoon Fitow (2013). *J. Geophys. Res. Atmos.* **2019**. [[CrossRef](#)]
23. Stoelinga, M.T.; Hobbs, P.V.; Mass, C.F.; Locatelli, J.D.; Colle, B.A.; Houze, R.A., Jr.; Rangno, A.L.; Bond, N.A.; Smull, B.F.; Rasmussen, R.M.; et al. Improvement of microphysical parameterization through observational verification experiment. *Bull. Am. Meteorol. Soc.* **2003**, *84*, 1807–1826. [[CrossRef](#)]
24. Zhang, G.; Sun, J.; Brandes, E.A. Improving Parameterization of Rain Microphysics with Disdrometer and Radar Observations. *J. Atmos. Sci.* **2006**, *63*, 1273–1290. [[CrossRef](#)]
25. Shan, Y.; Wilcox, E.M.; Gao, L.; Lin, L.; Mitchell, D.L.; Yin, Y.; Zhao, T.; Zhang, L.; Shi, H.; Gao, M. Evaluating Errors in Gamma-Function Representations of the Raindrop Size Distribution: A Method for Determining the Optimal Parameter Set for Use in Bulk Microphysics Schemes. *J. Atmos. Sci.* **2020**, *77*, 513–529. [[CrossRef](#)]
26. Chandrasekar, V.; Meneghini, R.; Zawadzki, I. Global and local precipitation measurements by radar. *Meteorol. Monogr.* **2003**, *52*, 215–236. [[CrossRef](#)]
27. Ryzhkov, A.V.; Giangrande, S.E.; Schuur, T.J. Rainfall Estimation with a Polarimetric Prototype of WSR-88D. *J. Appl. Meteorol.* **2005**, *44*, 502–515. [[CrossRef](#)]
28. Liu, L.P.; Zheng, J.F.; Ruan, Z.; Cui, Z.H.; Hu, Z.Q.; Wu, S.H.; Dai, G.Y.; Wu, Y.H. Comprehensive radar observations of clouds and precipitation over the Tibetan Plateau and preliminary analysis of cloud properties. *J. Meteorol. Res.* **2015**, *29*, 546–561. [[CrossRef](#)]
29. Chang, Y.; Guo, X. Characteristics of convective cloud and precipitation during summer time at Naqu over Tibetan Plateau (in Chinese). *Chin. Sci. Bull.* **2016**, *61*, 1706–1720. [[CrossRef](#)]
30. Wu, Y.H.; Liu, L.P. Statistical characteristics of raindrop size distribution in the Tibetan Plateau and southern China. *Adv. Atmos. Sci.* **2017**, *34*, 727–736. [[CrossRef](#)]
31. Porcù, F.; D’Adderio, L.P.; Prodi, F.; Caracciolo, C. Rain drop size distribution over the Tibetan Plateau. *Atmos. Res.* **2014**, *150*, 21–30. [[CrossRef](#)]
32. Jaffrain, J.; Berne, A. Experimental quantification of the sampling uncertainty associated with measurements from PARSIVEL disdrometers. *J. Hydrometeorol.* **2011**, *12*, 352–370. [[CrossRef](#)]
33. Battaglia, A.; Rustemeier, E.; Tokay, A.; Blahak, U.; Simmer, C. PARSIVEL snow observations: A critical assessment. *J. Atmos. Ocean. Technol.* **2010**, *27*, 333–344. [[CrossRef](#)]
34. Yuter, S.E.; Kingsmill, D.E.; Nance, L.B.; Löffler-Mang, M. Observations of precipitation size and fall speed characteristics within coexisting rain and wet snow. *J. Appl. Meteorol.* **2006**, *45*, 1450–1464. [[CrossRef](#)]
35. Huo, Z.; Ruan, Z.; Wei, M.; Ge, R.; Li, F.; Ruan, Y. Statistical characteristics of raindrop size distribution in south China summer based on the vertical structure derived from VPR-CFMCW. *Atmos. Res.* **2019**, *222*, 47–61. [[CrossRef](#)]
36. Tapiador, F.J.; Checa, R.; de Castro, M. An experiment to measure the spatial variability of rain drop size distribution using sixteen laser disdrometers. *Geophys. Res. Lett.* **2010**, *37*, L16803. [[CrossRef](#)]

37. Jaffrain, J.; Berne, A. Quantification of the small-scale spatial structure of the raindrop size distribution from a network of disdrometers. *J. Appl. Meteorol. Climatol.* **2012**, *51*, 941–953. [[CrossRef](#)]
38. Friedrich, K.; Higgins, S.; Masters, F.J.; Lopez, C.R. Articulating and stationary PARSIVEL disdrometer measurements in conditions with strong winds and heavy rainfall. *J. Atmos. Ocean. Technol.* **2013**, *30*, 2063–2080. [[CrossRef](#)]
39. Kalina, E.A.; Friedrich, K.; Ellis, S.M.; Burgess, D.W. Comparison of disdrometer and X-band mobile radar observations in convective precipitation. *Mon. Weather Rev.* **2014**, *142*, 2414–2435. [[CrossRef](#)]
40. Konwar, M.; Das, S.K.; Deshpande, S.M.; Chakravarty, K.; Goswami, B.N. Microphysics of clouds and rain over the Western Ghat. *J. Geophys. Res. Atmos.* **2014**, *119*, 6140–6159. [[CrossRef](#)]
41. Zhang, A.; Hu, J.; Chen, S.; Hu, D.; Liang, Z.; Huang, C.; Xiao, L.; Min, C.; Li, H. Statistical Characteristics of Raindrop Size Distribution in the Monsoon Season Observed in Southern China. *Remote Sens.* **2019**, *11*, 432. [[CrossRef](#)]
42. Lee, M.; Lin, P.; Chang, W.; Seela, B.K.; Janapati, J. Microphysical characteristics and types of precipitation for different seasons over north Taiwan. *J. Meteorol. Soc. Jpn.* **2019**, *97*, 841–865. [[CrossRef](#)]
43. Luo, L.; Xiao, H.; Yang, H.; Chen, H.; Guo, J.; Sun, Y.; Feng, L. Raindrop size distribution and microphysical characteristics of a great rainstorm in 2016 in Beijing, China. *Atmos. Res.* **2020**, *239*. [[CrossRef](#)]
44. Hopper, L.J.; Schumacher, C.; Humes, K.; Funk, A. Drop-size distribution variations associated with different storm types in southeast Texas. *Atmosphere* **2019**, *11*, 8. [[CrossRef](#)]
45. Serio, M.A.; Carollo, F.G.; Ferro, V. Raindrop size distribution and terminal velocity for rainfall erosivity studies. A review. *J. Hydrol.* **2019**, *576*, 210–228. [[CrossRef](#)]
46. Ma, Y.; Ni, G.; Chandra, C.V.; Tian, F.; Chen, H. Statistical characteristics of raindrop size distribution during rainy seasons in the Beijing urban area and implications for radar rainfall estimation. *Hydrol. Earth Syst. Sci.* **2019**, *23*, 4153–4170. [[CrossRef](#)]
47. Villalobospuma, E.; Martinezcastro, D.; Floresrojas, J.L.; Saavedrahuanca, M.; Silvavidal, Y. Diurnal cycle of raindrops size distribution in a valley of the Peruvian Central Andes. *Atmosphere* **2019**, *11*, 38. [[CrossRef](#)]
48. Zeng, Q.; Zhang, Y.; Lei, H.; Xie, Y.; Gao, T.; Zhang, L.; Wang, C.; Huang, Y. Microphysical characteristics of precipitation during pre-monsoon, monsoon, and post-monsoon periods over the South China Sea. *Adv. Atmos. Sci.* **2019**, *36*, 1103–1120. [[CrossRef](#)]
49. Checa-Garcia, R.; Tokay, A.; Tapiador, F. Binning effects on in-situ raindrop size distribution measurements. *Atmos. Meas. Tech.* **2014**, *7*, 2339–2379. [[CrossRef](#)]
50. Campos, E.; Zawadzki, I. Instrumental uncertainties in Z-R Relations. *J. Appl. Meteorol.* **1969**, *39*, 1088–1102. [[CrossRef](#)]
51. Löffler-Mang, M.; Joss, J. An optical disdrometer for measuring size and velocity of hydrometeors. *J. Atmos. Ocean. Technol.* **2000**, *17*, 130–139. [[CrossRef](#)]
52. Sheppard, B.; Joe, P. Comparison of raindrop size distribution measurements by a Joss-Waldvogel disdrometer, a PMS 2DG spectrometer, and a POSS doppler radar. *J. Atmos. Ocean. Technol.* **1994**, *11*, 874–887. [[CrossRef](#)]
53. Mallet, C.; Barthes, L. Estimation of gamma raindrop size distribution parameters: Statistical fluctuations and estimation errors. *J. Atmos. Ocean. Technol.* **2009**, *26*, 1572–1584. [[CrossRef](#)]
54. Tokay, A.; Petersen, W.A.; Gatlin, P.; Wingo, M. Comparison of raindrop size distribution measurements by collocated disdrometers. *J. Atmos. Ocean. Technol.* **2013**, *30*, 1672–1690. [[CrossRef](#)]
55. De Moraes Frasson, R.P.; da Cunha, L.K.; Krajewski, W.F. Assessment of the Thies optical disdrometer performance. *Atmos. Res.* **2011**, *101*, 237–255. [[CrossRef](#)]
56. Wen, L.; Zhao, K.; Zhang, G.; Liu, S.; Chen, G. Impacts of instrument limitations on estimated raindrop size distribution, radar parameters, and model microphysics during Mei-Yu season in East China. *J. Atmos. Ocean. Technol.* **2017**, *34*, 1021–1037. [[CrossRef](#)]
57. Krajewski, W.F.; Kruger, A.; Caracciolo, C.; Golé, P.; Barthes, L.; Creutin, J.-D.; Delahaye, J.-Y.; Nikolopoulos, E.I.; Ogden, F.; Vinson, J.-P. DEVEX-disdrometer evaluation experiment: Basic results and implications for hydrologic studies. *Adv. Water Resour.* **2006**, *29*, 311–325. [[CrossRef](#)]
58. Thurai, M.; Gatlin, P.; Bringi, V.N.; Petersen, W.; Kennedy, P.; Notaroš, B.; Carey, L. Toward completing the raindrop size spectrum: Case studies involving 2D-video disdrometer, droplet spectrometer, and polarimetric radar measurements. *J. Appl. Meteorol. Clim.* **2017**, *56*, 877–896. [[CrossRef](#)]

59. Guyot, A.; Pudashine, J.; Protat, A.; Uijlenhoet, R.; Pauwels, V.R.N.; Seed, A.; Walker, J.P. Effect of disdrometer type on rain drop size distribution characterisation: A new dataset for south-eastern Australia. *Hydrol. Earth Syst. Sci.* **2019**, *23*, 4737–4761. [[CrossRef](#)]
60. Atlas, D.; Srivastava, R.C.; Sekhon, R.S. Doppler radar characteristics of precipitation at vertical incidence. *Rev. Geophys. Space Phys.* **1973**, *11*, 1–35. [[CrossRef](#)]
61. Johnson, R.W.; Kliche, D.V.; Smith, P.L. Comparison of estimators for parameters of gamma distributions with left-truncated samples. *J. Appl. Meteorol. Climatol.* **2011**, *50*, 296–310. [[CrossRef](#)]
62. Johnson, R.W.; Kliche, D.V.; Smith, P.L. Maximum likelihood estimation of gamma parameters for coarsely binned and truncated raindrop size data. *Q. J. R. Meteorol. Soc.* **2013**, *140*, 1245–1256. [[CrossRef](#)]
63. Smith, P.L.; Kliche, D.V. The bias in moment estimators for parameters of drop-size distribution functions: Sampling from exponential distributions. *J. Appl. Meteorol.* **2005**, *44*, 1195–1205. [[CrossRef](#)]
64. Tokay, A.; Short, D.A. Evidence from tropical raindrop spectra of the origin of rain from stratiform versus convective clouds. *J. Appl. Meteorol.* **1996**, *35*, 355–371. [[CrossRef](#)]
65. Testud, J.; Oury, S.; Amayenc, P.; Black, R.A. The concept of “normalized” distributions to describe raindrop spectra: A tool for cloud physics and cloud remote sensing. *J. Appl. Meteorol.* **2001**, *40*, 1118–1140. [[CrossRef](#)]
66. Nzeukou, A.; Sauvageot, H.; Ochou, A.D.; Kebe, C.M.F. Raindrop size distribution and radar parameters at Cape Verde. *J. Appl. Meteorol.* **2004**, *43*, 90–105. [[CrossRef](#)]
67. Ulbrich, C.W.; Atlas, D. Rainfall microphysics and radar properties: Analysis methods for drop size spectra. *J. Appl. Meteorol.* **1998**, *37*, 912–923. [[CrossRef](#)]
68. Brandes, E.A.; Zhang, G.; Vivekanandan, J. An evaluation of a drop distribution-based rainfall estimator. *J. Appl. Meteorol.* **2003**, *42*, 652–660. [[CrossRef](#)]
69. Sharma, S.; Konwar, M.; Sarma, D.K.; Kalapureddy, M.C.R.; Jain, A.R. Characteristics of rain integral parameters during tropical convective, transition, and stratiform rain at gadanki and its application in rain retrieval. *J. Appl. Meteorol. Clim.* **2009**, *48*, 1245–1266. [[CrossRef](#)]
70. Jin, Q.; Yuan, Y.; Liu, H.J.; Shi, C.E.; Li, J.B. Analysis of microphysical characteristics of the raindrop spectrum over the area between the Yangtze River and the Huaihe River during summer. *Acta Meteorol. Sin.* **2015**, *73*, 778–788. [[CrossRef](#)]
71. Marshall, J.S.; Palmer, W.M.K. The distribution of raindrops with size. *J. Meteorol.* **1948**, *5*, 165–166. [[CrossRef](#)]
72. Fulton, R.A.; Breidenbach, J.P.; Seo, D.-J.; Miller, D.A. The WSR-88D rainfall algorithm. *Weather Forecast* **1998**, *13*, 377–395. [[CrossRef](#)]
73. Maki, M.; Keenan, T.D.; Sasaki, Y. Characteristics of the raindrop size distribution in tropical continental squall lines observed in Darwin, Australia. *J. Appl. Meteorol.* **2001**, *40*, 1393–1412. [[CrossRef](#)]
74. Moumouni, S.; Gosset, M.; Houngrinou, E. Main features of rain drop size distributions observed in Benin, West Africa, with optical disdrometers. *Geophys. Res. Lett.* **2008**, *35*, L23807. [[CrossRef](#)]
75. Chen, B.; Hu, W.; Pu, J. Characteristics of the raindrop size distribution for freezing precipitation observed in southern China. *J. Geophys. Res.* **2011**, *116*, D06201. [[CrossRef](#)]
76. Ji, L.; Chen, H.; Li, L.; Chen, B.; Xiao, X.; Chen, M.; Zhang, G. Raindrop size distributions and rain characteristics observed by a PARSIVEL disdrometer in Beijing, Northern China. *Remote Sens.* **2019**, *11*, 1479. [[CrossRef](#)]

